Tectonics

New Constraints on the Evolution of the Inner Northern Apennines by K-Ar Dating of Late Miocene-Early Pliocene Compression on the Island of Elba, Italy

Giulio Viola[1] (iD), Espen Torgersen[2,3] (iD), Francesco Mazzarini[4] (iD), Giovanni Musumeci[4,5] (iD), Roelant van der Lelij[2], Jasmin Schönenberger[2], and Paolo Stefano Garofalo[1]

[1]Department of Biological, Geological and Environmental Sciences, Università degli Studi di Bologna, Bologna, Italy, [2]Geological Survey of Norway, Trondheim, Norway, [3]Department of Geosciences and Petroleum, Norwegian University of Science and Technology, Trondheim, Norway, [4]Istituto Nazionale di Geofisica e Vulcanologia, Pisa, Italy, [5]Dipartimento di Scienze della Terra, Università di Pisa, Pisa, Italy

Abstract The Northern Apennines (NA) orogenic wedge formed during Oligocene-Miocene convergence and westward subduction of Adria beneath the European Plate. Extension ensued in the Mid-Late Miocene in response to Adria roll-back, causing opening of the back-arc Northern Tyrrhenian Sea. Whether extension continues uninterrupted since the Mid-Late Miocene or it was punctuated by short-lived compressional events, remains, however, uncertain. We used the K-Ar method to date a set of brittle-ductile and brittle deformation zones from the Island of Elba to contribute to this debate. We dated the low-angle Zuccale Fault (ZF), the Capo Norsi-Monte Arco Thrust (CN-MAT), and the Calanchiole Shear Zone (CSZ). The CN-MAT and CSZ are moderately west dipping, top-to-the-east thrusts in the immediate footwall of the ZF. The CSZ slipped 6.14 ± 0.64 Ma (<0.1 μm fraction) and the CN-MAT 4.90 ± 0.27 Ma ago (<0.4 μm fraction). The ZF, although cutting the two other faults, yielded an older age of 7.58 ± 0.11 Ma (<0.1 μm fraction). The ZF gouge, however, contains an illitic detrital contaminant from the Paleozoic age flysch deformed in its hanging wall and the age thus is a maximum faulting age. Removal of ~1% of a 300-Ma-old contaminant brings the ZF faulting age to <4.90 Ma. Our results provide the first direct dating of brittle deformation in the Apennines, constraining Late Miocene-Early Pliocene regional compression. They call for a refinement of current NA geodynamic models in the framework of the Northern Tyrrhenian Sea extension.

1. Introduction

The Italian inner Northern Apennines (NA; Figure 1a) are an orogenic wedge formed in response to the Upper Cretaceous-Eocene closure of the Ligurian-Piedmont ocean (Marroni et al., 2017, and references therein, for a comprehensive review) and the subsequent Oligocene-Miocene convergence and collision between the Adriatic Promontory and the Sardinia-Corsica Block, of African and European origin, respectively (e.g., Boccaletti et al., 1971; Vai & Martini, 2001 and references therein). Alternative models of subduction polarity exist (see Molli, 2008 for a review). Post-Eocene subduction and westward underthrusting of the Adriatic lithosphere progressively widened the NA wedge, with its compressional thrust front steadily migrating eastward to its current location at the base of the foreland Po Plain foothills and immediately offshore the eastern coast of central Italy. The NA hinterland includes the back-arc Northern Tyrrhenian Sea and several marine, transitional, and continental Mid-Late Miocene to Pliocene basins from eastern Corsica to western Tuscany (e.g., Jolivet et al., 1998). Back-arc crustal extension is generally defined as having begun in the Mid-Late Miocene in response to Adriatic slab roll-back, although the details of this evolution are still being lively debated. Uncertainties remain on the structural framework in which the back-arc basins formed. In particular, the debate hinges around whether they are grabens and half-grabens accommodating uninterrupted regional extension since the Miocene (Brogi, 2011; Martini & Sagri, 1993; Trevisan, 1950), or, instead, are at least in part infilled flexures formed and reworked also during short-lived compressive events ensued during the local post-Miocene evolution. These compressive events would have punctuated and repeatedly interrupted the syn- Miocene to post-Miocene regional extensional history (Boccaletti et al., 1999; Bonini et al., 2014; Bonini & Sani, 2002; Musumeci et al., 2008).
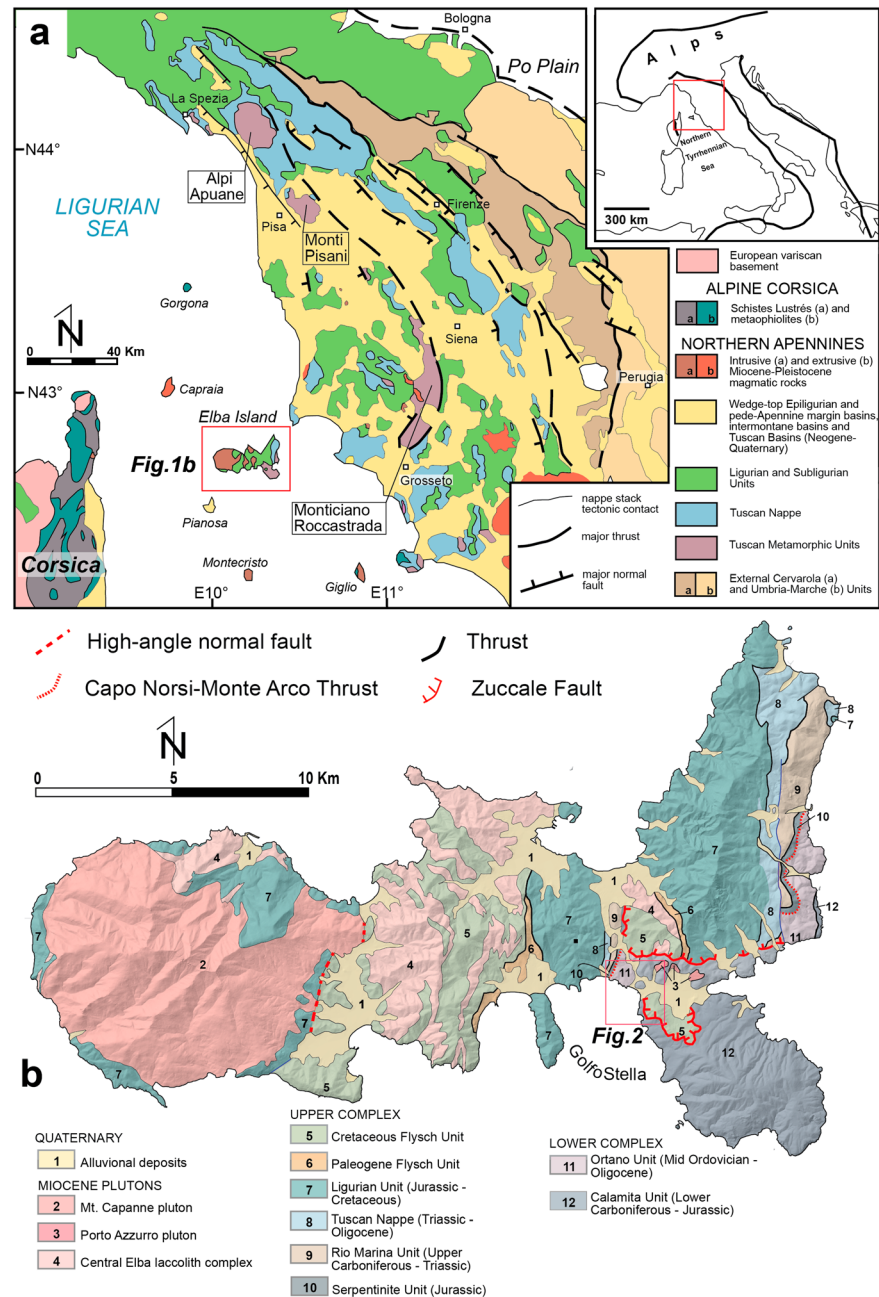
Figure 1. (a) Sketch geological map of the Northern Apennines and northern Corsica. The red box locates the Island of Elba, shown in detail in Figure 1b. (b) Simplified geological map of the Island of Elba. The Capo Norsi-Monte Arco Thrust and the Zuccale Fault are mapped in red.

The first-order geodynamic boundary conditions of the buildup and tearing down of the orogenic wedge are thus still weakly constrained, and the ongoing debate essentially reflects the poorly understood geological expression of the relationships between the NE vergent compressive evolution of the belt and the subsequent, and basically coaxial, extension leading to the opening of the Tyrrhenian Sea. Agreement exists, on the other hand, on the present-day extensional setting of the hinterland and the central domain of the Apennines, which accounts for the diffuse seismogenic character of that portion of the belt (e.g., Chiarabba & De Gori, 2016).

The easternmost Island of Elba (Figures 1a and 1b) is well suited to study in detail the complexities of the Neogene tectonic framework of the inner NA as it exposes a well-preserved section of the wedge. The

nappe pile outcropping there formed by eastward thrusting, stacking, and folding of oceanic and continental units during subduction from the Eocene and continuing to the Middle Miocene (e.g., Bortolotti et al., 2001; Keller & Coward, 1996; Trevisan, 1950, and references therein). Intrusive and volcanic rocks between 8.4 and 3.8 Ma in age crop out extensively in the northern Tyrrhenian Sea and in Tuscany (see reviews by Peccerillo, 2005, 2017; Serri et al., 1993, 2001, and references therein; Gagnevin et al., 2011). On Elba, these rocks are represented by the approximately 8.0–7.0 Ma Monte Capanne monzogranite and Central Elba Sill Complex (Figure 1b; e.g., Barboni et al., 2015; Dini et al., 2002; Westerman et al., 2004) and by the approximately 6.5 Ma Porto Azzurro monzogranitic pluton (Figure 1b; e.g., Gagnevin et al., 2011). The latter is exposed at only a few localities on easternmost Elba, where it pierces through the nappe stack, remaining otherwise shallowly buried. The Miocene-Pliocene magmatism of the inner NA is commonly interpreted as reflecting major crustal extension related to the coeval opening of the back-arc northern Tyrrhenian Sea (e.g., Boccaletti & Guazzone, 1972; Jolivet et al., 1998). Extension on the Island of Elba is traditionally associated with emplacement of the Monte Capanne and Porto Azzurro plutons (Westerman et al., 2004) and tectonic elision along the renowned Zuccale Fault (ZF; Collettini & Holdsworth, 2004) as a consequence of the northern Tyrrhenian sea opening (e.g., Keller & Coward, 1996; Jolivet et al., 1998). The ZF is interpreted as a major low-angle normal fault whose Late Miocene activity would have greatly facilitated regional E-W stretching and aided the Tyrrhenian opening (e.g., Collettini & Holdsworth, 2004; Keller & Pialli, 1990; Smith et al., 2011).

The activity of the ZF is considered coeval or slightly younger than the formation of the nearby Fe-skarn ore deposits 6.4–5.3 Ma (Tanelli et al., 2001), which represent a distinct, structurally-controlled hydrothermal event that involved a large tract of eastern Elba.

In the context of the lively debate mentioned above, although the school of thought advocating continuous extension from the Miocene remains by far the most credited (e.g., Jolivet et al., 1998), recent studies lend progressively more support to important, short-lived post-Miocene inversion episodes. This view is based on a range of structural evidence including:

1. Mesoscopic compressive structures controlling basement reactivation as well as growth and subsequent shortening of Miocene and Pliocene basins sedimentary infill, particularly in western Tuscany, but also in Corsica (e.g., Benvenuti et al., 2014; Bonini et al., 2014; Bonini & Sani, 2002; Cerrina Feroni et al., 2006; Fellin et al., 2005; Musumeci et al., 2008; Sani et al., 2009). Several seismic profiles also document numerous thrust faults and compressive features affecting the hinterland (e.g., Finetti et al., 2001).
2. Field evidence suggesting that the emplacement of some of the Miocene and Pliocene plutons of the Tuscan Archipelago in the Northern Tyrrhenian Sea and in western Tuscany occurred within overall compression (Mazzarini et al., 2011; Musumeci et al., 2005);
3. Detailed structural studies suggesting an alternative, compressive scenario for the ZF (Musumeci et al., 2015).

The overall coherence of the evidence listed above suggests that addressing the possibility of a post-Miocene inversion in the NA and Elba is important to the correct understanding of the geodynamic framework of the Apennine orogeny, of the Northern Tyrrhenian Sea, and of the dynamic behavior of orogenic wedges at large.

To contribute to this ongoing debate, we present a new data set of K-Ar radiometric dates of synkinematic illite from brittle to brittle-ductile fault rocks from selected faults of eastern Elba whose age was previously assumed to be Early Miocene. With this study we aim to (i) date thrust faults that contributed to the formation of the Apenninic orogenic wedge and elucidate their temporal relationship to the orogenic extension of the NA and the ZF and (ii) test the reliability and further refine the applicability of K-Ar dating of illite to Neogene deformation episodes. Indeed, the recent advances in integrated K-Ar dating of brittle faults that have allowed direct chronological constraints to be placed on complex and long-lived brittle strain localization histories were mostly possible through the study of Mesoproterozoic and Paleozoic structures, while generally overlooking more recent deformation histories (e.g., Scheiber & Viola, 2018; Torgersen et al., 2014, 2015; Viola et al., 2013, 2016). We show here that by means of careful characterization of the dated material, it is possible to reliably date also Miocene and Pliocene fault rocks, thus contributing to the understanding of the tectonic evolution of recent and active orogens.
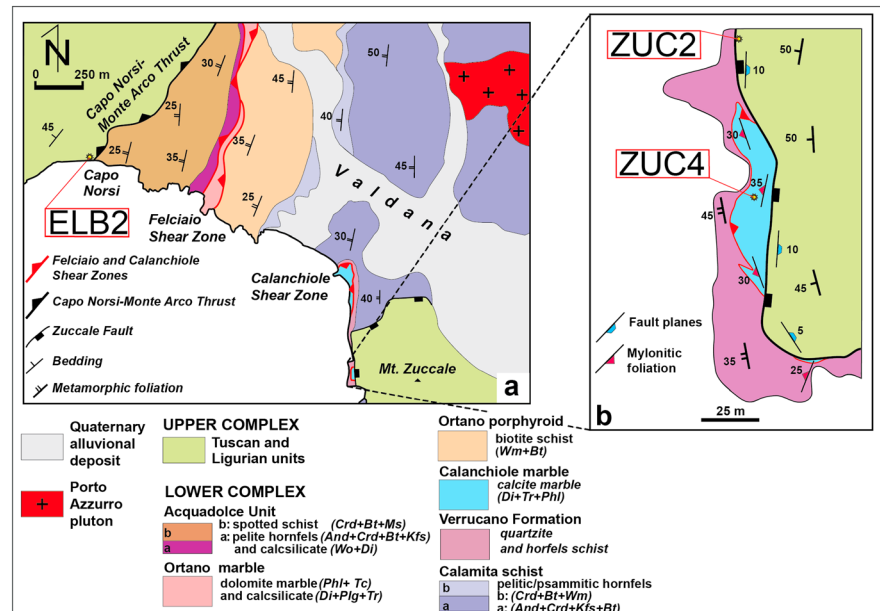
Figure 2. Detailed geological map of the study area along the northeastern shore of Golfo Stella and location of dated samples. The main brittle and brittle-ductile deformation zones of the area are indicated. (a) Location of sample ELB2 in the serpentinitic and nonmetamorphic hanging wall of the Capo Norsi-Monte Arco Thrust. (b) Blow-up of the Punta di Zuccale area, with the details of the local geology and the accurate location of samples ZUC2 and ZUC4. The Lower Complex is affected by contact metamorphism within the western side of the Porto Azzurro contact aureole (Crd: cordierite; Bt: biotite; Ms: muscovite; And: andalusite; Kfs: K feldspar; Wo: wollastonite; Di: diopside; Phl: phlogopite; Tc: talc; Plg: plagioclase; Tr: tremolite; Wm: white mica).

2. Geological Setting and Sample Material

The study area is along the eastern shore of "Golfo Stella" on the eastern Island of Elba (Figures 1b and 2), where the NA orogenic wedge is formed by a large, N-S trending and generally west dipping monocline formed by imbricated kilometric thrust sheets of both continental and oceanic affinity. Tectonic slivers therein are separated by west dipping, top-to-the-east thrusts. For the purpose of this study, we adopt a simplified classification of the nappe stack, which can be subdivided into an Upper and a Lower Complex separated by the Capo Norsi-Monte Arco Thrust (CN-MAT), a N-S trending and west dipping, top-to-the-east thrust fault. A Mid-Ordovician basement with Jurassic-Oligocene cover rocks and a Carboniferous basement with Triassic-Jurassic metasediments (referred to as Ortano and Calamita Unit, respectively; e.g., Musumeci et al., 2011; Papeschi et al., 2017) form the footwall to the CN-MAT. Their regional metamorphic grade reaches greenschist to upper amphibolite facies. The hanging wall is composed of lithologically heterogeneous and variably deformed Cretaceous and Paleogene Flysch and the oceanic-derived Ligurian Unit tectonically juxtaposed against the Triassic-Oligocene Tuscan Nappe and the Carboniferous-Triassic Rio Marina Formation of continental affinity. Imbrication during the Early Miocene is considered responsible for nappe stack formation by thrusting and folding (e.g., Massa et al., 2017, and references therein) and juxtaposition of greenschist- to blueschist-facies tectonic units within the exposed tectonostratigraphy (Bianco et al., 2015).

The thermal signature of the study area (Figure 2a) is complicated by the local static overprint due to the medium-grade thermal aureole of the Porto Azzurro monzogranite. As documented by Musumeci and Vaselli (2012), the Lower Complex preserves And + Crd + Bt + Ms contact metamorphism, with the metamorphic grade gradually decreasing to the west with increasing distance from the Porto Azzurro pluton (Figure 2a). Musumeci et al. (2015) dated the contact metamorphic event in the study area to 6.76 ± 0.08 and 6.33 ± 0.07 Ma by ^{40}Ar/^{39}Ar on phlogopite and muscovite, from a marble and a schist unit, respectively.

The nappe stack is discordantly cut and displaced by up to 6 km to the east by the low-angle ZF (e.g., Collettini & Holdsworth, 2004; Keller & Pialli, 1990; Musumeci et al., 2015; Smith & Faulkner, 2010), which

deforms all structures and rocks of the nappe stack as well as the Porto Azzurro pluton thermal aureole (Figures 1b and 2). Although the ZF is traditionally described and interpreted as a subhorizontal to gently dipping top-to-the-east low-angle normal fault, Musumeci et al. (2015) proposed an alternative model wherein the exposed ZF is the flat of a much larger, out-of-sequence top-to-the-east thrust that cuts through the nappe stack. The same authors bracketed the activity of the ZF between 6.23 ± 0.06 and 5.39 ± 0.46 Ma, as constrained by the youngest available muscovite $^{40}Ar/^{39}Ar$ age from the footwall and a U-Th-He age on adularia and specularite from hematite mineralizations in the hanging wall (e.g., Lippolt et al., 1995).

In an attempt to add much needed geochronological constraints to the structuring and later reworking of this portion of the NA orogenic wedge, we sampled three fault zones from the area (Figure 2):

1. Capo Norsi-Monte Arco Thrust (CN-MAT), a major brittle fault zone of the orogenic wedge (Figures 1 and 2a). The sampled fault is within the serpentinites of the Ligurian Units, dips 30–35° to the west, and represents a subsidiary fault strand of the master CN-MAT (Figures 2a and 3a). An approximately 15-cm-thick gouge layer defining the fault core contains serpentinite clasts up to several centimeters in diameter dispersed within a fine-grained clay-rich matrix. (Figures 3a and 3b). *Sample ELB2* (UTM coordinates Zone 33 N, WGS 84, 10.34269°E, 42.76539°N) is from the clay-rich, dark green gouge from the lowermost exposed part of the core (red patch in Figure 3a). Kinematic indicators, such as imbricated or sigmoidal clasts and Riedel fractures, invariably indicate top-to-the-east thrusting and there is no evidence of significant structural reactivation localized along the sampled interval (Figure 3b). Extensive, hydrofracturing-related and serpentine-filled veins are present in both footwall and hanging wall of the thrust, which consistently truncates them (Figures 3a and 3b). As also reported by Musumeci and Vaselli (2012), the serpentinite is thrusted along the CN-MAT over the contact-metamorphic rocks of the Porto Azzurro thermal aureole. The CN-MAT hanging wall, however, is not contact metamorphosed, thus requiring thrusting to be younger than the approximately 6.5 Ma emplacement of the Porto Azzurro monzogranite.
2. Calanchiole Shear Zone (CSZ; Figures 2a and 2b), a 40–45° west dipping and top-to-the-east, brittle-ductile thrust deforming Jurassic carbonates (Garfagnoli et al., 2005; Musumeci & Vaselli, 2012) that are contact-metamorphosed into hornfels by the Porto Azzurro pluton. Musumeci and Vaselli (2012) and Papeschi et al. (2017) provide a detailed description of the CSZ, whose core is defined by calcite mylonites recrystallized with stable tremolite and talc defining millimetric layers oriented parallel to the mylonitic foliation. *Sample ZUC4* (Figures 3c and 3d; UTM coordinates Zone 33 N, WGS 84, 10.3580°E, 42.75349°N) is from a discrete, few centimeter-thick brittle-ductile level within the CSZ. Kinematic indicators such as small-scale imbricates, sigmoidal clasts, and shear bands confirm top-to-the-east shearing.
3. Zuccale Fault (ZF; Figures 1 and 2a and 2b), whose low-angle brittle component cuts across discordantly the two previous faults in the footwall and an Upper Cretaceous flysch in the hanging wall (e.g., Musumeci et al., 2015). At the sampling location, the ZF dips very gently to the west. *Sample ZUC2* (Figure 3e; UTM coordinates Zone 33 N, WGS 84, 10.3580°E, 42.7540°N) is from a N-S trending section at Punta di Zuccale (Figures 2a and 2b), where the ZF consists of an up to 2-m-thick brittle fault zone defined by matrix-supported breccias and greyish cataclasites containing centimetric gouge layers (e.g., Musumeci et al., 2015). ZUC2 is a clay-rich gouge formed at the expense of the hanging wall Cretaceous flysch and was sampled from immediately above a discrete main slip surface containing E-W trending subhorizontal slickenlines (Figure 3f). As documented by Musumeci et al. (2015), ZF-related cataclasites contain clasts of monzogranitic composition derived from the Porto Azzurro pluton, which constrains the last brittle slip along the fault to after magma crystallization at c. 6.5 Ma. Given the outcrop geometric relationships, whereby the ZF cuts geometrically across both the CSZ and the CN-MAT, sample ZUC2 should be the youngest.

3. Analytical Methods and Sample Characterization

The analytical procedures for separating, characterizing, and dating the samples are described in detail and represent the current routine workflow at the recently established laboratory for clay characterization and K-Ar dating at the Geological Survey of Norway, Trondheim.

Untreated fault sample material was weighed and loaded into HD-PE plastic bottles within which samples were completely submerged in Type II water (15 MΩ resistivity). The bottles were sealed in a shrink-wrap plastic envelope and placed in a Julabo F38-ME cryostatic bath filled with ethylene glycol and subjected to
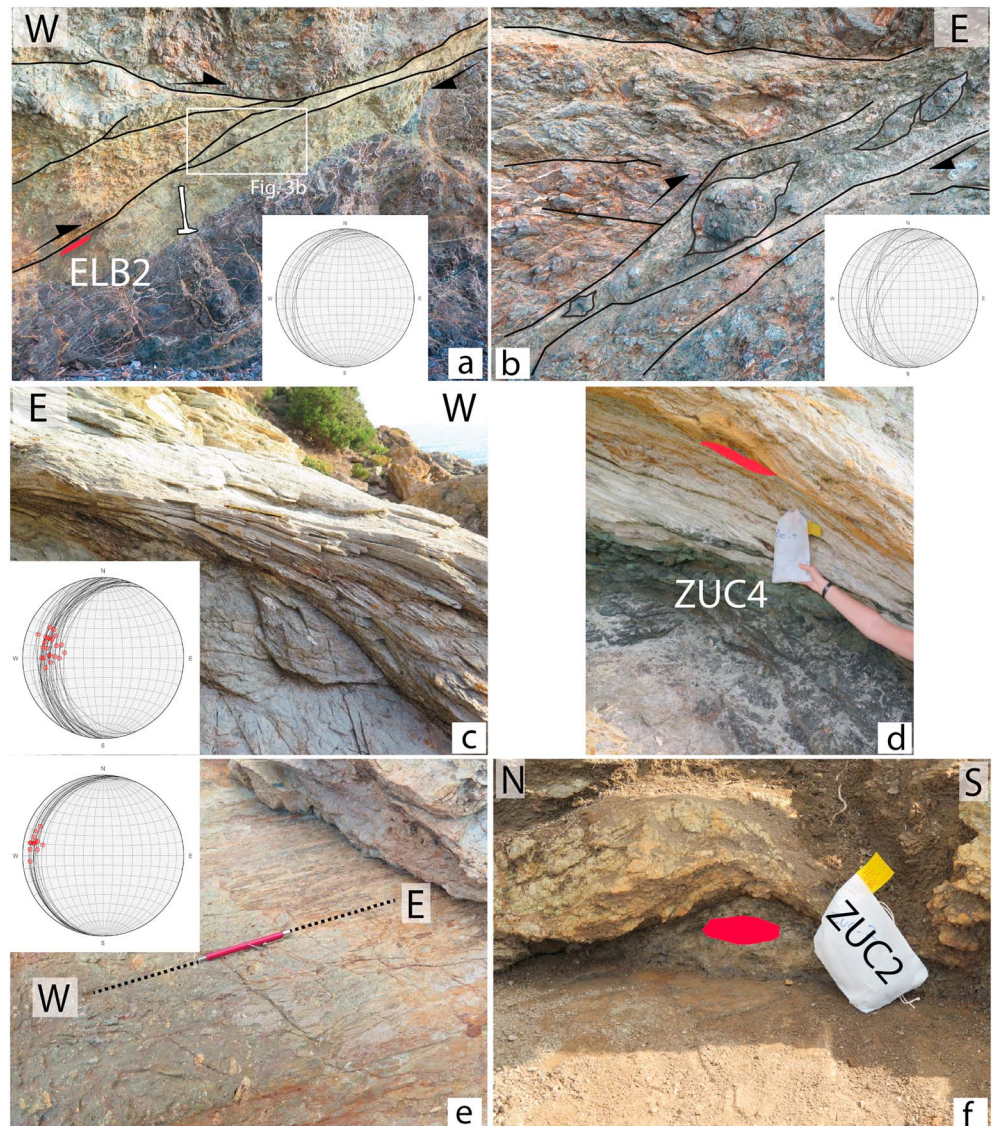
Figure 3. (a) Capo Norsi-Monte Arco Thrust (CN-MAT): The pale yellow layout highlights the moderately *W*/WNW dipping brittle fault core. Note the Riedel shears indicating reverse kinematics. The ELB2 red polygon shows the exact location of the dated ELB2 sample. Stereonet: lower hemisphere, equal area projection of brittle slip planes. (b) Detail of the area highlighted in Figure 3a. Individual clasts within the locally foliated cataclasites have sigmoidal shapes and are locally imbricated to confirm overall top-to-the east thrusting. Stereonet: lower hemisphere, equal area projection of cataclastic foliation. (c) West dipping mylonitic foliation planes asymptotically dragged into a discrete top-to-the-east brittle-ductile thrust plane of the Calanchiole Shear Zone (CSZ). Shearing deformed Jurassic carbonates that were contact-metamorphosed into hornfels with stable tremolite and talc defining millimetric layers oriented parallel to the mylonitic foliation. Stereonet: lower hemisphere, equal area projection of mylonitic foliation (great circles) and stretching lineation (red dots). (d) The ZUC4 red polygon shows the exact location of the dated ZUC4 sample from a discrete, only a few cm thick brittle-ductile level within the CSZ. (e) Main slip, top-to-the east striated plane of the Zuccale Fault (ZF) immediately below the ZUC2 sample of (f). Stereonet: great circles: low-dip slip planes of the fault at the sampling locality. Red dots: striations.

at least one month of cyclic temperature oscillations between −12 and +25 °C with a 2-hr hold time at each temperature (>100 cycles). This allowed water to infiltrate between the particles and disaggregate them gently by gelifraction, without resulting in artificial grain size reduction. Subsequently, the finer than sand fractions of the disaggregated samples were transferred to graduated cylinders using Type II pure water, and the <2 μm, 2–6 μm, and 6–10 μm fractions were successively isolated using Stokes' law. Two or more successive separations were performed to increase the yield of the <2 μm suspensions.

The <2 μm suspensions were centrifuged with a Beckman-Coulter Avanti J-26S XP centrifuge fitted with a JCF-Z continuous flow rotor and a calibrated Cole Parmer peristaltic pump, to separate 0.1–0.4 μm and <0.1 μm fractions. To generate <0.4 μm solutions, the centrifuge was run at 3700 RPM with a suspension flow-through rate of 400 ml/min, resulting in <0.4 μm supernatant suspensions and 0.4–2 μm solid pellets. The <0.4-μm suspensions were then centrifuged at 10.000 RPM with a solution flow-through rate of 180 ml/min to generate <0.1 μm supernatant suspensions and 0.1–0.4 μm solid pellets. The <0.1 μm supernatants were subsequently collected by centrifugation in a Beckman-Coulter Avanti J-26S XP centrifuge equipped with a JA-10 rotor, at 9500 RPM for 65 min, to collect the remaining <0.1 μm fractions as solid pellets. The <0.1 μm, 0.1–0.4 μm, 0.4–2 μm, 2–6 μm, and 6–10 μm grain size fractions were dried in an oven at 45 ± 10 °C. The centrifugation routine was calibrated and checked using LPS-PIDS with a Beckman Coulter LS13-320 particle size analyzer fitted with an aqueous liquid module.

Air-dried, homogenized clay materials and standards were wrapped in folded molybdenum microcapsules, and the net mass of the aliquots was determined using a Mettler Toledo XPE26DR microbalance equipped with an antistatic ionizer. The microbalance has resolution of 2 μg and a measured uncertainty of 4 μg (1σ) for the total weighing procedure. The clays and standards were left overnight in a drying oven at 85 ± 3 °C, and weighed again to determine the dry weight and relative humidity loss. The molybdenum envelopes were subsequently loaded into an ultrahigh vacuum extraction line and baked at a maximum temperature of 120 °C to eliminate excess water following the recommendations of Clauer and Chaudhuri (1995).

Argon was extracted from the samples in a Pond Engineering double vacuum resistance furnace at 1400 °C for 20 min. During heating, bulk sample gas was expanded directly into a stainless steel vessel housing a freshly activated Titanium Sublimation Pump, to strip the sample gas from a majority of reactive gases including H_2O, N, O_2, CO, and CO_2 (O'Hanlon, 2003). A known molar amount of approximately 2×10^{-13} moles of pure ^{38}Ar spike (Schumacher, 1975) was prepared using a 0.2 cc gas pipette attached to a 4000 cc reservoir and was equilibrated with the purified sample gas. The gas mixture was subsequently isolated in a second cleanup stage and exposed for 10 min to two SAES GP50 getter cartridges with ST101 Zr-Al alloy, one of which was kept at 350 °C and one at room temperature, to remove residual reactive gases including H_2 and CH_4.

Argon isotopes were determined on an IsotopX NGX multicollector noble gas mass spectrometer in multicollector mode. Faraday cups with 10^{12} Ω amplifiers were used to measure ^{36}Ar and ^{38}Ar, and a faraday cup with a 10^{11} Ω amplifier was used to measure ^{40}Ar. Time-zero beam intensities were measured for 30 cycles of twenty 1-s integrations, and time-zero intensities were calculated using exponential regressions back to gas inlet time. Furnace blanks were run regularly between samples and had $^{40}Ar/^{36}Ar$ compositions close to atmospheric argon (Lee et al., 2006). Instrument mass discrimination was determined using aliquots of argon purified from air and compared with the reference value of 298.56 ± 0.31 (Lee et al., 2006). The ^{38}Ar spike pipette was calibrated using GA-1550 biotite with $^{40}Ar^* = 1.342 \pm 0.007 \times 10^{-9}$ mol/g (McDougall and Wellman, 2011) and HD-B1 biotite (Fuhrmann et al., 19871987) with a $^{40}Ar^* = 3.351 \pm 0.01 \times 10^{-10}$ mol/g (Charbit et al., 1998). The overall standard deviation of the pooled spike calibrations by combined GA1550 and HD-B1 is <0.3%. The accuracy of the $^{40}Ar^*$ determinations was monitored within run by GA-1550 and HD-B1 biotite.

K concentration was determined by digesting a sample aliquot of ~5.5–50 mg in $Li_2B_4O_7$ flux at a temperature of 1000 ± 50 °C in Pd crucibles. The resulting glass was subsequently dissolved in HNO_3 and analyzed on a Perkin Elmer Optima 4300 DV ICP-OES. 1σ uncertainties are estimated from the reproducibility of a range of standards with K concentrations between 0.19% K and 8.3% K and take into account the signal strength of K during analysis. Mean standard deviations of all measured standards overlap with published reference values within their published uncertainties.

K-Ar ages were calculated using the ^{40}K decay constants, abundance, and branching ratio of Steiger and Jäger (1977). Atmospheric Ar corrections were performed using the relative abundances of ^{40}Ar, ^{38}Ar and ^{36}Ar of Lee et al. (2006). Age uncertainties were estimated using the error equation for multicollector isotope dilution measurements from Hałas and Wójtowicz (2014) modified to take into account the uncertainty on mass discrimination.

X-ray diffraction (XRD) analyses were performed on a Bruker D8 Advance with LynxEye detector. Measurement parameters were used as follows: Cu Kα radiation, 40 kV/40 mA, scan range 3–75 °2θ (2–40 °2θ for clays), step size 0.02 °2θ, time/step 1 s, fixed divergence slit 0.6 mm (1 mm for clays), primary and secondary soller slits 2.5 °, Ni-filter, knife edge, and sample rotation 1/30 s. Randomly prepared specimens were used for semiquantification, whereas oriented specimens on glass slide were studied for clay identification. These were prepared by letting 1 ml of sample suspension dry out on a glass slide. The slides were analyzed at room temperature, after 24 hr glycolization and after heat treatment at 500 °C for 1 hr.

4. Results

All ages are reported in Table 1 and are plotted in Figure 4a. Four size fractions were separated and dated by K-Ar analysis from sample ZUC4, from 2–6 μm to <0.1 μm. Ages range between 12.62 ± 1.29 Ma, for the coarsest, and 6.14 ± 0.64 Ma for the finest fraction, all being statistically identical except the age of the coarsest fraction. Four fractions ranging between 6–10 μm and <0.4 μm were also dated from sample ELB2. A duplicate split of the <0.4 μm was also dated for reproducibility. The obtained ages range between 7.02 ± 0.37 Ma for the coarsest and the two statistically identical 5.11 ± 0.36 and 4.90 ± 0.27 Ma for the finest and its duplicate. No <0.1 μm fraction could be separated from ELB2. Finally, five fractions were dated for sample ZUC2, from the coarsest 6–10 μm to the finest <0.1 μm. Ages define an inclined spectrum in the sense of Pevear (1999), wherein the coarsest fraction yields the oldest age of 43.12 ± 0.77 Ma and the finest the youngest age of 7.58 ± 0.11 Ma, with the ages of the intermediate size fractions decreasing with grain size between these two end members (Figure 4a).

All dated fractions were studied with XRD except for the finest ones of samples ZUC2 and ELB2 (Table 2), which did not yield sufficient material. All fractions of ZUC4, i.e., the hornfels of the CSZ, have a very similar composition dominated by amphibole and talc. Chlorite and smectite are present in all fractions. Calcite occurs abundantly in the coarsest fraction, but progressively decreases with decreasing grain size and is not present in the finest fraction. Illite/muscovite was not detected by XRD in any of the fractions, but minor amounts of platy, authigenic, and synkinematic chlorite-smectite mixed layers were imaged by scanning electron microscope, confirming the presence of small amounts of K-bearing clay phases in the smallest fractions, which were below the XRD detection limit (Figure 4b). In addition, the sample has an extremely low K content, with all fractions containing <0.1 wt% K (Table 1), which is consistent with the carbonatic origin of the rock and which accounts for its relatively large age uncertainty.

All fractions of ELB2, the faulted serpentinites of the CN-MAT, show rather poor crystallinity resulting in broad XRD peaks with low intensity. They contain abundant chlorite, smectite, and chlorite-smectite mixed layers with the latter increasing with decreasing grain size. Amphibole and zeolite are minor components. Smectite and chlorite-smectite mixed layer minerals are the K-bearing phases in this sample in addition to very small amounts of illite-smectite, which, however, remain below the XRD detection limit and were only detected by energy-dispersive X-ray spectroscopy (EDS) analysis at the scanning electron microscope.

Sample ZUC2 is the most heterogeneous from a compositional point of view, which agrees with the gouge developing at the expense of the Cretaceous flysch in the hanging wall of the ZF. All fractions comprise abundant quartz, dolomite, and kaolinite. Illite/muscovite and illite-smectite mixed layers are predominant, with the smectitic proportion considerably increasing with decreasing grain size. Detailed transmission electron microscope (TEM) imaging and associated EDS were carried out to verify the presence of illite in the finest fraction, as this was not studied by XRD due to a lack of material. Interestingly, illite occurs in the <0.1 μm fraction with two distinct morphological types. The most common type is needles and fibers (Figure 4c). Less common, yet significant (see discussion below), are tiny, euhedral platelets up to 200 nm in diameter (Figure 4d).

5. Discussion

K-Ar dating was carried out on synkinematic illite separated into multiple grain sizes to discriminate the role of clay synkinematic authigenesis and, thus, to date the last increment of recorded slip and assess the potential for earlier deformation. Our results provide new inputs to the ongoing debate concerning the post-Miocene geodynamic evolution of the NA and constrain beyond any reasonable doubt the existence of at

Table 1
K-Ar Results

Size fraction (μm)	^{40}Ar* (mol/g)	σ (^{40}Ar*) (%)	^{40}Ar*/^{40}Artot (%)	K (wt%)	σ (K) (%)	Age (Ma)	σ (Age) (Ma)
ELB-2: Capo Norsi-Monte Aro Thrust (CN-MAT); 33 N, WGS 84, 10.34269°E, 42.76539°N							
ELB-2 < 0.4 μm	1.140E−12	2.24	1.08	0.134	5	4.90	0.27
ELB-2 < 0.4 μm duplicate	1.189E−12	5.01	0.91	0.134	5	5.11	0.36
ELB-2 < 2 μm	1.607E−12	1.19	1.41	0.201	5	4.60	0.24
ELB-2 2-6 μm	1.551E−12	1.20	1.51	0.147	5	6.07	0.31
ELB-2 6-10 μm	1.313E−12	1.47	1.44	0.108	5	7.02	0.37
ZUC-4: Calanchiole Shear Zone, UTM33N, WGS84, 10.3580°E, 42.75349°N							
ZUC-4 < 0.1 μm	7.155E−13	2.74	0.75	0.067	10	6.14	0.64
ZUC-4 < 0.4 μm	6.705E−13	2.48	1.30	0.054	10	7.12	0.73
ZUC-4 < 2 μm	5.278E−13	4.41	1.82	0.043	10	7.03	0.77
ZUC-4 2–6 μm	9.753E−13	2.17	1.61	0.044	10	12.62	1.29
ZUC-2: Zuccale Fault (ZF), UTM33N, WGS 84, 10.3580°E, 42.7540°N							
ZUC-2 < 0.1 μm	6.831E−11	0.31	14.10	5.18	1.4	7.58	0.11
ZUC-2 < 0.4 μm	1.464E−10	0.29	28.39	5.48	1.4	15.34	0.21
ZUC-2 < 2 μm	2.107E−10	0.29	48.06	4.37	1.5	27.58	0.41
ZUC-2 2–6 μm	1.988E−10	0.29	57.46	3.18	1.6	35.69	0.58
ZUC-2 6–10 μm	1.568E−10	0.29	64.17	2.07	1.8	43.12	0.77
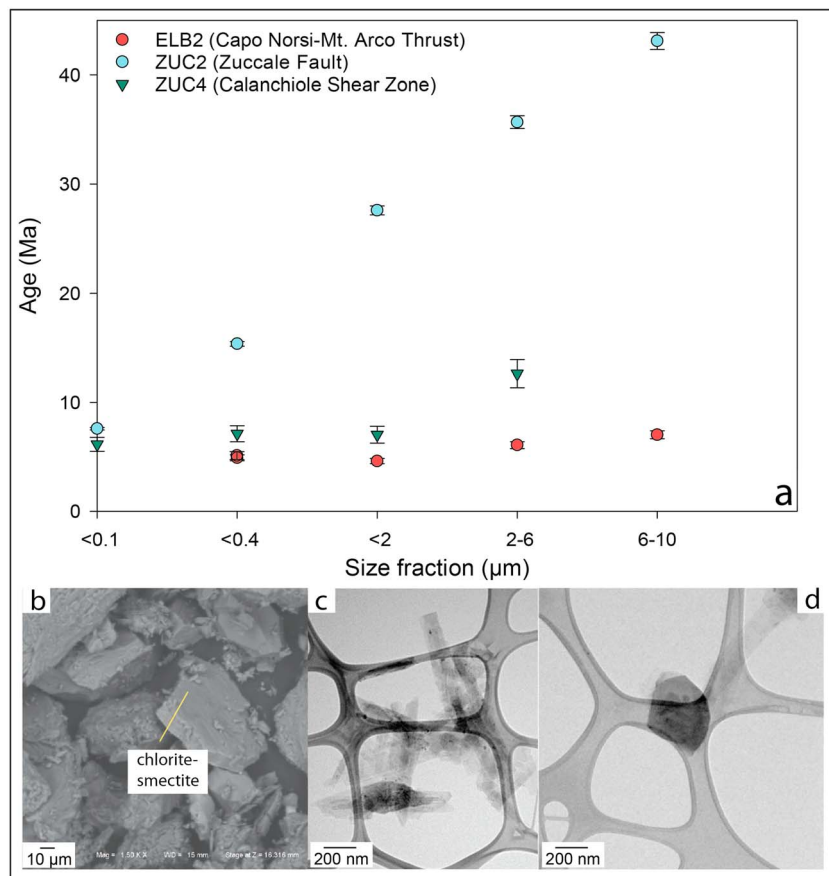
Figure 4. (a) K-Ar age versus grain size spectra for the three dated samples. Note the significant slope of the curve defined by sample ZUC2 as opposed to the flat-lying age-grain size curves for the other two samples. (b) Scanning electron microscope image of platy chlorite-smectite crystal in sample ZUC4. (c and d) Different habits for two generations of illite both contained in the finest fraction of sample ZUC2 as confirmed by EDS (energy dispersive spectroscopy) analysis and imaging at the TEM (transmission electron microscope). The acicular shape of the crystals in (c) is typical of authigenic, synkinematic crystals, whereas the platy shape of (d) is typical of a protolithic, detrital crystal.

Table 2
X-ray Diffraction Results

Sample	Fraction	qtz	dol	cal	kutn	amph	zeo	tlc	brk	ill/musc *and* ill-sm	kln	chl	sm	chl-sm
ELB2	<2 μm					x	x					xxxx	xxxx	xxx
ELB2	2–6 μm					xx	traces					xxxx	xxxx	xxx
ELB2	6–10 μm					xx	traces					xxxx	xxxx	xx
ZUC4	<0.1 μm					xxxx		xx				xxx	x	
ZUC4	<0.4 μm			traces		xxxx		xx				xx	xx	
ZUC4	<2 μm			x		xxxx		x				xx	x	
ZUC4	2–6 μm			xx		xxxx		x				xx	x	
ZUC2	<0.4 μm									xxxx	traces			
ZUC2	<2 μm	xxxx	x							xxxx	x			
ZUC2	2–6 μm	xxxx	x		traces				x	xxx (x)	x			
ZUC2	6–10 μm	xxxx	xx		x				x	xxx	x			

Note. Mineral abbreviations: qtz, quartz; dol, dolomite; cal, calcite; kutn, kutnohorite; amph, amphibole; zeo, zeolite; tlc, talc; brk, brookite; ill/musc and ill-sm, illite/ muscovite and illite-smectite mixed layer; kln, kaolinite; chl, chlorite; sm, smectite; chl-sm, chlorite-smectite mixed layer. Semiquantification of mineral concentrations (wt%): x < 5, xx 5–15, xxx 15–30, xxxx >30.

least one tectonic compressive event of Late Miocene-Pliocene age, as recorded by samples ZUC4 and ELB2 from the CSZ and CN-MAT, respectively.

The ages from all dated fractions for those two samples define a remarkable flat "age versus grain-size" curve (Figure 4), with only the 2–6 μm fraction of sample ZUC4 being slightly older than the other ages (Table 1). According to the Age Attractor Model by Torgersen et al. (2014) and Viola et al. (2016), this is indicative of the presence of only one dominant generation of illite for all dated fractions, which seemingly formed during one single episode of deformation. Given the general absence of K-bearing phases in serpentinites and marbles, we conclude that the K-bearing dated illite formed authigenically and synkinematically within the two faults. The older ages for the two coarsest fractions in each sample reflect minute quantities therein of protolithic K-bearing minerals (Torgersen et al., 2015; Table 1). The obtained ages therefore reliably constrain the age of brittle slip along the CSZ at 6.14 ± 0.64 Ma (<0.1 μm fraction of sample ZUC4) and along the CN-MAT at 4.90 ± 0.27 Ma (<0.4 μm fraction of sample ELB2). Since the finest size fractions of both samples are
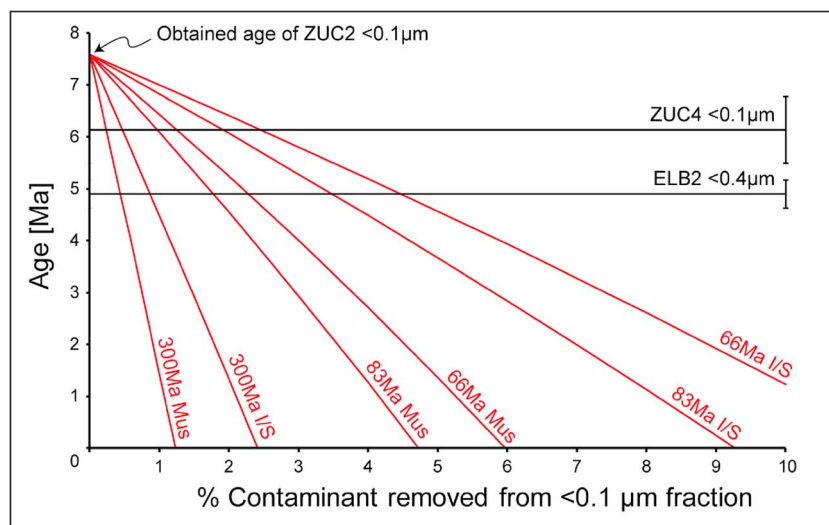

Figure 5. Two end-member contamination calculations to assess the impact on the age of ZUC2 < 0.1 μm by the possible presence of varying amounts of K-bearing protolithic muscovite and illite/smectite (I/S). The red curves show how the age of the fraction changes as a function of the amount of contaminant removed. The curves are calculated assuming protolithic grains with Carboniferous (300 Ma) or Upper Cretaceous (83–66 Ma) K-Ar ages, and with ideal muscovite (9.81% K) and representative I/S (5% K) compositions. The black lines show the obtained age and standard deviation of the finest size fraction of the two other fault samples for reference.
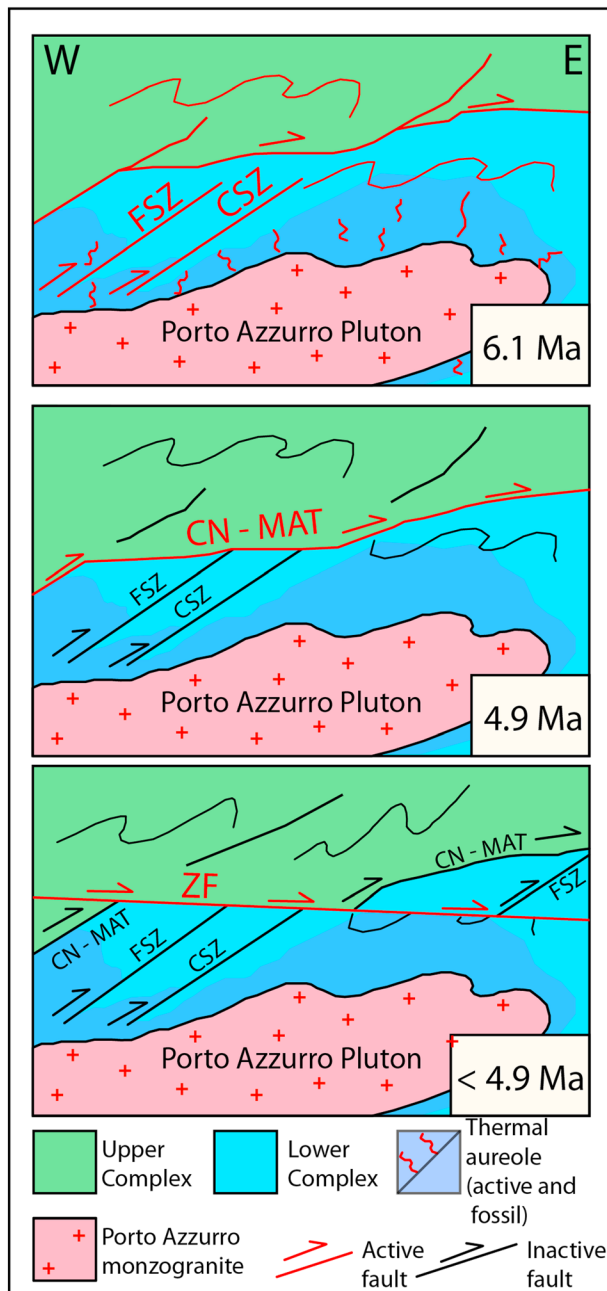
Figure 6. Simplified conceptual model for a revised evolution of the study area depicting three dated stages of deformation, corresponding to the age of the Calanchiole Shear Zone (CSZ), of the Capo Norsi-Monte Arco Thrust (CN-MAT), and Zuccale Fault (ZF), respectively. Compression is suggested by our structural and geochronological approach, leading to a model for the inner Apennines based on Late Miocene-Pliocene compression interrupting an earlier regional extensional phase, which is instead generally believed to act uninterrupted since at least the Late Miocene.

statistically identical (<2, <0.4, and <0.1 μm for ZUC4 and <2, <2D, and <0.4 μm for ELB2; Table 1), weighted mean ages may be calculated, yielding 6.70 ± 0.41 Ma for ZUC4 and 4.81 ± 0.16 Ma for ELB2. By combining these ages with our structural observations—which exclude significant structural reactivation—we conclude that brittle deformation along the CSZ and the CN-MAT was accommodated during one top-to-the-east thrusting event. These results are fully consistent with independent geological observations by Musumeci and Vaselli (2012), who described the internal imbrication of part of the thermal aureole leading to the repetition of the contact metamorphic facies by thrusting along the Felciaio Shear Zone (Figure 2), a west dipping synmetamorphic top-to-the-east thrust that closely resembles in its geometry and kinematic framework the CN-MAT and the CSZ. The age of contact metamorphism in the area was dated to between 6.76 ± 0.08 and 6.33 ± 0.07 Ma by $^{40}Ar/^{39}Ar$ dating of phlogopite and muscovite of a marble and a spotted schist unit, respectively (Musumeci et al., 2015). The CSZ K-Ar illite age is statistically identical to the age of contact metamorphism, which implies synmetamorphic deformation. The CSZ therefore contributed by thrusting to the repetition of the metamorphic zonation of the Porto Azzurro aureole, as suggested by Musumeci and Vaselli (2012). The 4.90 ± 0.27 Ma age of the CN-MAT, which is younger than that of contact metamorphism, is fully compatible with the observed juxtaposition of nonmetamorphic rocks in the hanging wall of the CN-MAT against the Porto Azzurro metamorphic aureole in the footwall (Musumeci & Vaselli, 2012).

We exclude partial or total resetting of the obtained illite K-Ar ages by the heat of the Porto Azzurro pluton because the dated samples still yield statistically distinct ages, in spite of their close geographical location.

As mentioned above, the ZF cuts discordantly the west dipping CSZ and CN-MAT. Its radiometric ages should therefore be younger than the ages from the other fault zones. However, the ZF yields the oldest finest fraction of the three samples at 7.58 ± 0.11 Ma. We studied this apparent discrepancy through a careful analysis of our analytical results.

Noteworthy is that sample ZUC2 is a compositionally heterogeneous gouge (Table 2) that formed from the frictional deformation of a Cretaceous flysch in the immediate hanging wall of the fault. Additional TEM imaging and EDS analysis was performed on the finest fraction of ZUC2 to study the morphological and compositional characteristics of illite therein. The coexistence of fibrous and platy illites (Figures 4c and 4d) suggests that the measured K-Ar date records contributions from two illite populations, which likely formed at distinct times. While fibrous habits are expression of true authigenesis, possibly synkinematic, platy crystals, in addition to in situ authigenesis under specific conditions (e.g., Torgersen et al., 2014), may also indicate a contaminant component (typically muscovite) inherited from the wall rock that is reworked within the gouge. The coexistence of both illite types in the dated fractions of ZUC2 (Figures 4c and 4d) suggests that even the finest fraction, which hosts the highest amount of authigenic and synkinematic

illite, still contains a mixture of protolithic and authigenic illite and that, therefore, the obtained age has to be regarded as a maximum age for faulting. That age still belongs to a mixing line between the old coarsest fraction and the "true" faulting age.

In detail, the ZUC2 gouge formed at the expense of an upper Cretaceous arenaceous flysch (Marina di Campo Fm.; Raggi et al., 1965; Aiello et al., 1977) of Campanian-Maastrichtian age (83–66 Ma, Parea, 1964). This

turbiditic deposit contains clastic mineral grains (quartz, K-feldspar, plagioclase, and mica) and also lithic fragments from metamorphic, volcanic, and sedimentary rocks derived from a Paleozoic basement (Aiello et al., 1977). Clastic mica (muscovite, biotite, and chlorite grains) ranges between 2.4 and 14% (same authors). According to Aiello et al. (1977), the lithostratigraphic sequence and mineral/rock fragment composition the Marina di Campo Fm. may suggest a correlation with the turbiditic formations of the internal Ligurian Units (e.g., Mt. Gottero Fm.) derived from the Paleozoic continental margin of the "Corso-Sardo Massif" (Marroni et al., 1992).

To further constrain this scenario, we have performed simple two end-member contamination calculations to determine how the age of the finest fraction of ZUC2 would decrease by removing various amounts of a contaminant with moderate K content (5% K, representative of illite and illite/smectite) or with high K content (9.8%, representative of ideal muscovite) derived from the Cretaceous flysch. In addition to a Paleozoic contaminant (300 Ma K-Ar age), we have also run models with Upper Cretaceous contaminants (66 and 83 Ma K-Ar age). Figure 5 shows that as a function of the age of the contaminating phase, the removal of <5% of an Upper Cretaceous K-bearing contaminant and <1% of a Paleozoic contaminant would decrease the age of the finest fraction of ZUC2 gouge below 4.9 Ma, that is, the age of the CN-MAT thrust that is cut by the ZF.

Based on this calculation and considering the significant compositional heterogeneity of the dated gouge, we believe therefore that a contribution from clastic grains of Paleozoic phyllosilicates contained in the arenaceous flysch is indeed a plausible explanation of why the finest fraction of ZUC2 is slightly older than expected on the basis of geometric relationships.

The new ages are consistent with late Miocene nappe imbrication, folding and coeval magma emplacement in response to crustal shortening affecting the whole Elba Island nappe stack, as suggested by Mazzarini et al. (2011) and Musumeci & Vaselli, (2012; Figure 6). According to Musumeci and Vaselli (2012), the simultaneous deformation of different structural levels of the nappe stack (i.e., the CN-MAT between the upper and lower thrust complex and the FSZ and CSZ in the lower thrust complex; Figure 6) attests to widespread compressional tectonics ending with the eastward displacement of the nappe stack along the ZF. No significant deformation would be ascribable to the emplacement of the plutons (Papeschi et al., 2017). In central-eastern Elba, the geometry and kinematics of the studied structures, their spatial relationships and their new ages are thus consistent with the suggestion of important middle-late Miocene to early Pliocene large-scale out-of-sequence thrusting (Massa et al., 2017). While most of the thrusting was coeval with pluton emplacement (c. 6.1 Ma old CSZ), its last deformation increments postdated the pluton-related thermal anomaly (4.9 Ma old CNT-MAT; Figure 6).

The CN-MAT at the base of the upper thrust complex and the FSZ and CSZ in the lower thrust complex can thus be regarded as the expression of brittle and brittle-ductile to ductile deformation accommodated under low and medium-high temperature conditions, respectively, in response to the local thermal conditions. Indeed, in the Calamita Unit to the south of the study area Papeschi et al. (2017) reported clear evidence of a continuous transition from ductile to ductile-brittle and brittle deformation during the progressive fading of the pluton thermal perturbation.

In this complex tectonothermal framework, the ZF possibly accommodated the youngest increment of out of sequence thrusting that developed after 5 Ma, when the magma-related thermal anomaly had already faded and the nappe stack was exposed to temperatures between 120 and 150 °C for a geothermal gradient in the 20–25 ° C/km range and a maximum depth of 6 km for the lower portion of the currently exposed portion of the wedge. These temperature conditions are, in turn, consistent with the purely brittle deformation recorded by the ZF cataclasites and gouges (Musumeci et al., 2015).

In addition to these tectonic implications, we stress that the new illite ages are also consistent with the suggested relationships between deformation and hydrothermal activity in eastern Elba (Tanelli et al., 2001 and references therein). The close similarity between the 6.14 and 4.90 Ma range of faulting activity constrained here and the age of Fe-skarn formation as determined by previous work 6.4–5.3 Ma (Tanelli et al., 2001) indicates that the ZF was active at the time when Fe-rich hydrothermal fluids generated the nearby skarn deposits. This agrees well with the evidence of hydrothermal mineral precipitation within the foliated cataclasites of the ZF documented by Gundlach-Graham et al. (2018). These authors show that the dolomite-sphalerite-galena-Fe oxide-amorphous silica assemblage within the cataclasites is anomalously

enriched in As, Sb, In, Ga, and Ag, which provides compelling evidence for remarkable hydrothermal fluid flow within the ZF.

In a regional perspective, our new Late Miocene-Early Pliocene ages confirm the deformation of the Oligocene to Miocene NA wedge by out-of-sequence thrusting (see, for example, Boccaletti & Sani, 1998), which we interpret as the expression of a renewed shortening episode after early extension in response to initial slab roll-back (e.g., Bonini et al., 2014).

The ages of our study represent a first quantitative step toward the determination of an absolute time framework for the structuring of the NA orogenic wedge and also have implications for the age and the meaning of the so-called "Northern Tyrrhenian Sea extension," which is generally interpreted as due to the late Miocene slab roll-back of Adria (Rosenbaum & Lister, 2004 and references therein).

Our study confirms the possibility to date by K-Ar synkinematic illite formed by Neogene faulting. Fundamental, however, remains the careful mineralogical characterization of the samples and the detailed multiscalar structural investigation of the targeted faults. In comparison to Paleozoic and older faulting episodes, K-Ar dating of synkinematic clay formed during Neogene brittle deformation may require an even more careful mineralogical characterization of the dated material. This is necessary to discriminate the effects of K-bearing protolithic detrital phases, whose radiogenic signature may disturb significantly the geochronological results. As shown by the modeling of Figure 5, approximately 1% of a 300-Ma-old "contaminant" preserved within the finest fraction of sample ZUC2 is sufficient to make the ZF faulting older than faulting along structures clearly cut by the ZF.

6. Conclusions

Our results are fully consistent with existing geological data and provide the first isotopic dating of brittle deformation in the Apennines. In combination with field, kinematic, and regional geological considerations, they undoubtedly constrain a Late Miocene-Early Pliocene regional compressive state of stress in the NA, with the brittle ZF possibly being its latest expression. This compressional episode followed an earlier phase of upper crustal extension (e.g., Massa et al., 2017, specifically for eastern Elba and Bonini et al., 2014 for the NA), presumably active between approximately 17 and 14 Ma and was, in turn, followed by renewed extension. The latter is responsible for the current extensional state of the inner and central NA, where high-angle seismogenic faults contribute to the tearing down of the previously structured compressional orogenic wedge. The existence of Late-Miocene-Early Pliocene compression requires a reevaluation of the geodynamic models of the evolution of the NA orogenic wedge. In the light of our new structural data and geochronological constraints, therefore, it is necessary to aim at a better understanding of the relationships between the belt deep processes and the state of stress in the upper portion of the wedge. The classic "Northern Tyrrhenian Sea extension" paradigm also requires refining to allow the formulation of a new interpretative model that takes into account all the new geological data in the geodynamic framework of the central Mediterranean area.

An existing, significant data set for eastern Corsica, part of the Island of Elba and western Tuscany, supports indirectly post-Miocene compression (e.g., Fellin et al., 2005 for Corsica; Bonini et al., 2014 for a review in the Tuscan NA or Musumeci et al., 2015, for Elba), but our results are the first geochronological evidence of this complexity. Future similar geochronological studies from key structures of the belt will permit the creation of a tighter time framework for the evolution of the entire orogenic wedge through time and in space.

References

Aiello, E., Bruni, P., & Sagri, M. (1977). Depositi canalizzati nei flysch Cretacei dell'isola d'Elba. *Bollettino della Societa Geologica Italiana*, *96*, 297–329.

Barboni, M., Annen, C., & Schoene, B. (2015). Evaluating the construction and evolution of upper crustal magma reservoirs with coupled U/Pb zircon geochronology and thermal modeling: A case study from the Mt. Capanne pluton (Elba, Italy). *Earth and Planetary Science Letters*, *432*, 436–448. https://doi.org/10.1016/j.epsl.2015.09.043

Benvenuti, M., Del Conte, S., Scarselli, N., & Dominici, S. (2014). Hinterland basin development and infilling through tectonic and eustatic processes: Latest Messinian-Gelasian Valdelsa Basin, Northern Apennines, Italy. *Basin Research*, *26*(3), 387–402. https://doi.org/10.1111/bre.12031

Bianco, C., Brogi, A., Caggianelli, A., Giorgetti, G., Liotta, D., & Meccheri, M. (2015). HP-LT metamorphism in Elba Island: Implications for the geodynamic evolution of the inner Northern Apennines (Italy). *Journal of Geodynamics*, *91*, 13–25. https://doi.org/10.1016/j.jog.2015.08.001

Boccaletti, M., Bonini, M., Moratti, G., & Sani, F. (1999). Compressive Neogene-Quaternary tectonics in the hinterland area of the Northern Apennines. *Journal of Petroleum Geology*, 22(1), 37–60. https://doi.org/10.1111/j.1747-5457.1999.tb00458.x

Boccaletti, M., Elter, P., & Guazzone, R. (1971). Plate tectonics models for the development of Western Alps and Northern Apennines. *Nature*, 234, 108–111.

Boccaletti, M., & Guazzone, G. (1972). Gli archi appenninici, il Mar Ligure ed il Tirreno nel quadro della tettonica dei bacini marginali di retro-arco. *Memorie della Societa Geologica Italiana*, 11, 211–216.

Boccaletti, M., & Sani, F. (1998). Cover thrust reactivations related to internal basement involvement during Neogene-Quaternary evolution of the Northern Apennines. *Tectonics*, 17(1), 112–130. https://doi.org/10.1029/97TC02067

Bonini, M., & Sani, F. (2002). Extension and compression in the Northern Apennines (Italy) hinterland: Evidence from the late Miocene-Pliocene Siena-Radicofani Basin and relations with basement structures. *Tectonics*, 21(3), 1010. https://doi.org/10.1029/2001TC900024

Bonini, M., Sani, F., Stucchi, E. M., Moratti, G., Benvenuti, M., Menanno, G., & Tanini, C. (2014). Late Miocene shortening of the Northern Apennines back-arc. *Journal of Geodynamics*, 74, 1–31. https://doi.org/10.1016/j.jog.2013.11.002

Bortolotti, V., Fazzuoli, M., Pandeli, E., Principi, G., Babbini, A., & Corti, S. (2001). Geology of central and eastern Elba Island, Italy. *Ofioliti*, 26(2a), 97–150.

Brogi, A. (2011). Bowl-shaped basin related to low-angle detachment during continental extension: The case of the controversial Neogene Siena Basin (central Italy, Northern Apennines). *Tectonophysics*, 499(1-4), 54–76. https://doi.org/10.1016/j.tecto.2010.12.005

Cerrina Feroni, A., Bonini, M., Martinelli, P., Moratti, G., Sani, F., Montanari, D., & Del Ventisette, C. (2006). Lithological control on thrust-related deformation in the Sassa-Guardistallo Basin (Northern Apennines hinterland, Italy). *Basin Research*, 18(3), 301–321. https://doi.org/10.1111/j.1365-2117.2006.00295.x

Charbit, S., Guillou, H., & Turpin, L. (1998). Cross calibration of K–Ar standard minerals using an unspiked Ar measurement technique. *Chemical Geology*, 150(1-2), 147–159.

Chiarabba, C., & De Gori, P. (2016). The seismogenic thickness in Italy: Constraints on potential magnitude and seismic hazard. *Terra Nova*, 28(6), 402–408. https://doi.org/10.1111/ter.12233

Clauer, N., & Chaudhuri, S. (1995). Clays in crustal environments: Isotope tracing and dating (359 pp.). Berlin: Springer-Verlag.

Collettini, C., & Holdsworth, R. E. (2004). Fault zone weakening and character of slip along low-angle normal faults: Insights from the Zuccale fault, Elba, Italy. *Journal of the Geological Society*, 161(6), 1039–1051. https://doi.org/10.1144/0016-764903-179

Dini, A., Innocenti, F., Rocchi, S., Tonarini, S., & Westerman, D. S. (2002). The magmatic evolution of the late Miocene laccolith–pluton–dyke granitic complex of Elba Island, Italy. *Geological Magazine*, 139(3), 257–279.

Fellin, M. G., Picotti, V., & Zattin, M. (2005). Neogene to Quaternary rifting and inversion in Corsica: Retreat and collision in the western Mediterranean. *Tectonics*, 24, TC1011. https://doi.org/10.1029/2003TC001613

Finetti, I. R., Boccaletti, M., Bonini, M., Del Ben, A., Geletti, R., Pipan, M., & Sani, F. (2001). Crustal section based on CROP seismic data across the north Tyrrhenian-Northern Apennines-Adriatic Sea. *Tectonophysics*, 343(3-4), 135–163. https://doi.org/10.1016/S0040-1951(01)00141-X

Fuhrmann, U., Lippolt, H. J., & Hess, J. C. (1987). Examination of some proposed K-Ar standards: $^{40}Ar^{39}Ar$ analyses and conventional K/ Ar data: Chemical Geology. *Isotope Geoscience section*, 66(1-2), 41–51.

Gagnevin, D., Daly, J. S., Horstwood, M. S. A., & Whitehouse, M. J. (2011). In-situ zircon U–Pb, oxygen and hafnium isotopic evidence for magma mixing and mantle metasomatism in the Tuscan Magmatic Province, Italy. *Earth and Planetary Science Letters*, 305(1–2), 45–56. https://doi.org/10.1016/j.epsl.2011.02.039

Garfagnoli, F., Menna, F., Pandeli, E., & Principi, G. (2005). The Porto Azzurro unit (Mt. Calamita promontory, south eastern Elba Island, Tuscany): Stratigraphic, tectonic and metamorphic evolution. *Bollettino della Societa Geologica Italiana*, 3, 119–138.

Gundlach-Graham, A., Garofalo, P. S., Schwarz, G., Redi, D., & Günther, D. (2018). High-resolution, quantitative element imaging of an upper crust, low-angle Cataclasite (Zuccale Fault, Northern Apennines) by laser ablation ICP time-of-flight mass spectrometry. *Geostandards and Geoanalytical Research*. https://doi.org/10.1111/ggr.12233

Hałas, S., & Wójtowicz, A. (2014). Propagation of error formulas for K/Ar dating method. *Geochronometria*, 41(3), 202–206.

Jolivet, L., Faccenna, C., Goffé, B., Mattei, M., Rossetti, F., Brunet, C., et al. (1998). Midcrustal shear zones in postorogenic extension: Example from the northern Tyrrhenian Sea. *Tectonics*, 103(B6), 12,123–12,160.

Keller, J. V. A., & Coward, M. P. (1996). The structure and evolution of the northern Tyrrhenian Sea. *Geological Magazine*, 103, 1–16.

Keller, J. V. A., & Pialli, G. (1990). Tectonics of the Island of Elba: A reappraisal. *Bollettino della Societa Geologica Italiana*, 109, 413–425.

Lee, J. Y., Marti, K., Severinghaus, J. P., Kawamura, K., Yoo, H. S., Lee, J. B., & Kim, J. S. (2006). A redetermination of the isotopic abundances of atmospheric Arc. *Geochimica et Cosmochimica Acta*, 70(17), 4507–4512.

Lippolt, H. J., Wernicke, R. S., & Baehr, R. (1995). Paragenetic specularite and adularia (Elba, Italy): Concordand (U+Th)-He and K-Ar ages. *Earth and Planetary Science Letters*, 132(1-4), 43–51. https://doi.org/10.1016/0012-821X(95)00046-F

Marroni, M., Meneghini, F., & Pandolfi, L. (2017). A revised Subduction inception model to explain the late cretaceous, double-vergent orogen in the precollisional Western Tethys: Evidence from the Northern Apennines. *Tectonics*, 36, 2227–2249. https://doi.org/10.1002/2017TC004627

Marroni, M., Monechi, S., Perilli, N., Principi, G., & Treves, B. (1992). Late Cretaceous flysch deposits of the Northern Apennines, Italy: Age of inception of orogenesis-controlled sedimentation. *Cretaceous Research*, 13(5-6), 487–504. https://doi.org/10.1016/0195-6671(92)90013-G

Martini, I. P., & Sagri, M. (1993). Tectono-sedimentary characteristics of Late Miocene-Quaternary extensional basins of the Northern Apennines, Italy. *Earth-Science Reviews*, 34(3), 197–233. https://doi.org/10.1016/0012-8252(93)90034-5

Massa, G., Musumeci, G., Mazzarini, F., & Pieruccioni, D. (2017). Coexistence of contractional and extensional tectonics during the Northern Apennines orogeny: The late Miocene out-of-sequence thrust in the Elba Island nappe stack. *Geological Journal*, 52(3), 353–368. https://doi.org/10.1002/gj.2761

Mazzarini, F., Musumeci, G., & Cruden, A. R. (2011). Vein development during folding in the upper brittle crust: The case of tourmaline-rich veins of eastern Elba Island, northern Tyrrhenian Sea, Italy. *Journal of Structural Geology*, 33(10), 1509–1522. https://doi.org/10.1016/j.jsg.2011.07.001

McDougall, I., & Wellman, P. (2011). Calibration of GA1550 biotite standard for K/Ar and $^{40}Ar/^{39}Ar$ dating. *Chemical Geology*, 280(1-2), 19–25.

Molli, G. C. (2008). Northern Apennine Corsica orogenic system: An updated overview. In S. Siegesmund, B. Fugenschuh, & N. Froitzheim (Eds.), *Tectonic aspects of the Alpine-Dinaride-Carpathian System* (pp. 413–442). London: Geological Society, Special Publications.

Musumeci, G., Mazzarini, F., & Barsella, M. (2008). Pliocene crustal shortening on the Tyrrhenian side of the Northern Apennines: Evidence from the Gavorrano antiform (southern Tuscany, Italy). *Journal of the Geological Society*, 165(1), 105–114. https://doi.org/10.1144/0016-76492007-004

Musumeci, G., Mazzarini, F., Corti, G., Barsella, M., & Montanari, D. (2005). Magma emplacement in a thrust ramp anticline: The Gavorrano Granite (Northern Apennines, Italy). *Tectonics*, 24, TC6009. https://doi.org/10.1029/2005TC001801

Musumeci, G., Mazzarini, F., & Cruden, A. R. (2015). The Zuccale Fault, Elba Island, Italy: A new perspective from fault architecture. *Tectonics*, *34*, 1195–1218. https://doi.org/10.1002/2014TC003809

Musumeci, G., Mazzarini, F., Tiepolo, M., & Di Vincenzo, G. (2011). U-Pb and 40Ar-39Ar geochronology of Palaeozoic units in the Northern Apennines: Determining protolith age and Alpine evolution using the Calamita Schist and Ortano Porphyroid. *Geological Journal*, *46*(4), 288–310. https://doi.org/10.1002/gj.1266

Musumeci, G., & Vaselli, L. (2012). Neogene deformation and granite emplacement in the metamorphic units of Northern Apennines (Italy): Insights from mylonitic marbles in the Porto Azzurro pluton contact aureole (Elba Island). *Geosphere*, *8*(2), 470–490. https://doi.org/10.1130/GES00665.1

O'Hanlon, J. F. (2003). A user's guide to vacuum technology (516 pp.). New Jersey: John Wiley & Sons.

Papeschi, S., Musumeci, G., & Mazzarini, F. (2017). Heterogeneous brittle-ductile deformation at shallow crustal levels under high thermal conditions: The case of a synkinematic contact aureole in the inner Northern Apennines, southeastern Elba Island, Italy. *Tectonophysics*, *717*, 547–564. https://doi.org/10.1016/j.tecto.2017.08.020

Parea, G. C. (1964). Età e provenienza dei clastici del flysch arenaceo dell'isola d'Elba. *Accademia Nazionale Lincei, Classe Scienze Fisiche Matematiche e Naturali, Rendiconti, VIII* (XXXVI, 5).

Peccerillo, A. (2005). *Plio-Quaternary volcanism in Italy* (p. 365). Berlin-Heidelberg: Springer.

Peccerillo, A. (2017). *Cenozoic volcanism in the Tyrrhenian Sea Region* (p. 399). Germany: Springer.

Pevear, D. R. (1999). Illite and hydrocarbon exploration. *Proceedings of the National Academy of Sciences United States of America*, *96*(7), 3440–3446. https://doi.org/10.1073/pnas.96.7.3440

Raggi, G., Squarci, P., & Taffi, L. (1965). Considerazioni stratigrafico-tettoniche sul Flysch dell'isola d'Elba. *Bollettino della Societa Geologica Italiana*, *84*, 1–14.

Rosenbaum, G., & Lister, G. S. (2004). Neogene and Quaternary rollback evolution of the Tyrrhenian Sea, the Apennines, and the Sicilian Maghrebides. *Tectonics*, *23*, TC1013. https://doi.org/10.1029/2003TC001518

Sani, F., Bonini, M., Cerrina Feroni, A., Mazzarini, F., Moratti, G., Musumeci, G., et al. (2009). Messinian-Early Pliocene crustal shortening along the Tyrrhenian margin of Tuscany, Italy. *Italian Journal of Geosciences*, *128*(2), 593–604.

Scheiber, T., & Viola, G. (2018). Complex bedrock fracture patterns: A multipronged approach to resolve their evolution in space and time. *Tectonics*, *37*, 1030–1062. https://doi.org/10.1002/2017TC004763

Schumacher, E. (1975). Herstellung von 99, 9997% ^{38}Ar für die ^{40}K/^{40}Ar Geochronologie. *Geochronologia Chimia*, *24*, 441–442.

Serri, G., Innocenti, F., & Manetti, P. (1993). Geochemical and petrological evidence of the subduction of delaminated Adriatic continental lithosphere in the genesis of the Nogene-Quaternary magmatism of central Italy. *Tectonophysics*, *223*(1-2), 117–147. https://doi.org/10.1016/0040-1951(93)90161-C

Serri, G., Innocenti, F., & Manetti, P. (2001). Magmatism from Mesozoic to present: Petrogenesis, time-space distribution and geodynamic implications. In G. B. Vai & I. P. Martini (Eds.), *Anatomy of an orogen: the Apennines and Adjacent Mediterranean Basins* (pp. 77–104). Dordrecht, Netherlands: Kluver Academic Publishers.

Smith, S. A. F., & Faulkner, D. R. (2010). Laboratory measurements of the frictional properties of the Zuccale low-angle normal fault, Elba Island, Italy. *Journal of Geophysical Research*, *115*, B02407. https://doi.org/10.1029/2008JB006274

Smith, S. A. F., Holdsworth, R. E., Collettini, C., & Pearce, M. A. (2011). The microstructural character and mechanical significance of fault rocks associated with a continental low-angle normal fault: The Zuccale Fault, Elba Island, Italy. In Å. Fagereng, V. G. Toy, & J. V. Rawland (Eds.), *Geological Society of London Special Publication: Geology of the earthquake source: A volume in honour of Rick Sibson* (pp. 97–113). London: Geological Society.

Steiger, R., & Jäger, E. (1977). Subcommission on geochronology: Convention on the use of decay constants in geo-and cosmochronology. *Earth and Planetary Science Letters*, *36*(3), 359–362.

Tanelli, G., Benvenuti, M., Costagliola, P., Dini, A., Lattanzi, P., Maineri, C., et al. (2001). The iron mineral deposits of Elba island: State of the art. *Ofioliti*, *26*, 239–248.

Torgersen, E., Viola, G., Zwingmann, H., & Harris, C. (2014). Structural and temporal evolution of a reactivated brittle-ductile fault—Part II: Timing of fault initiation and reactivation by K-Ar dating of synkinematic illite/muscovite. *Earth and Planetary Science Letters*, *410*, 212–224.

Torgersen, E., Viola, G., Zwingmann, H., & Henderson, I. H. C. (2015). Inclined K-Ar illite age spectra in brittle fault gouges: Effects of fault reactivation and wall-rock contamination. *Terra Nova*, *27*(2), 106–113. https://doi.org/10.1111/ter.12136

Trevisan, L. (1950). L'Elba orientale e la sua tettonica di scivolamento per gravità. *Memorie Istituto Geologia Università Padova*, *16*, 5–39.

Vai, G. B., & Martini, I. P. (Eds.) (2001). *Anatomy of an orogen: The Apennines and Adjacent Mediterranean Basins* (p. 637). Dordrecht, Netherlands: Kluwer Academic Publishers.

Viola, G., Scheiber, T., Fredin, O., Zwingmann, H., Margreth, A., & Knies, J. M. (2016). Deconvoluting complex structural histories archived in brittle fault zones. *Nature Communications*, *7*, 13,448. https://doi.org/10.1038/ncomms13448

Viola, G., Zwingmann, H., Mattila, J., & Kapyaho, A. (2013). K-Ar illite age constraints on the Proterozoic formation and reactivation history of a brittle fault in Fennoscandia. *Terra Nova*, *25*(3), 236–244. https://doi.org/10.1111/ter.12031

Westerman, D. S., Dini, A., Innocenti, F., & Rocchi, S. (2004). Rise and fall of a nested Christmas-tree laccolith complex, Elba Island, Italy. In C. Breitkreuz & N. Petford (Eds.), *Physical Geology of High-Level Magmatic Systems* (pp. 195–213). London: Geological Society.